CRYSTAL GROWTH & DESIGN

pubs.acs.org/crystal

Article

# Evidence for Facilitated Surface Transport during Ge Crystal Growth by Indium in Liquid Hg–In Alloys at Room Temperature

Dhruba Pattadar, Quintin Cheek, Andrea Sartori, Yifan Zhao, Rajendra P. Giri, Bridget Murphy, Olaf Magnussen,* and Stephen Maldonado*

Cite This: *Cryst. Growth Des.* 2021, 21, 1645–1656

Read Online

ACCESS | Metrics & More | Article Recommendations | Supporting Information

**ABSTRACT:** Room-temperature electrodeposition of Ge crystallites was investigated by the electrochemical liquid–liquid–solid (ec-LLS) process using a family of $Hg_{1-x}In_x$ alloys. The objective was to determine whether different liquid metal alloys with nominally the same bulk solubility toward Ge but potentially different surface character would yield any differences in the resultant Ge crystallites. Variation of the In fraction in these alloys was the control variable. The following details were ascertained from the cumulative data. First, in accordance with thermodynamic predictions, the surface of $Hg_xIn_{1-x}$ alloys was strongly enriched with Hg according to X-ray specular reflectivity data. These data further indicated that the surface enrichment was confined exclusively to a single atomic layer at the liquid metal surface. These properties of the $Hg_{1-x}In_x$/electrolyte interface structure facilitated the first two steps of the ec-LLS process. Second, the presence of In influenced the morphology of the resultant Ge crystallites from ec-LLS, in accordance with mediated transport of the Ge upon initial electroreduction. Specifically, X-ray diffraction, Raman, and microscopy data suggest that a strong affinity between In and Ge that affects the crystal morphology. This study thus motivates further exploration of both In as a component in liquid metal solvents to facilitate grain size and more general studies detailing how the surface structure and composition of liquid metals influence crystal growth. These findings significantly advance the prospect for preparing technologically relevant inorganic crystalline semiconductors at low temperatures.

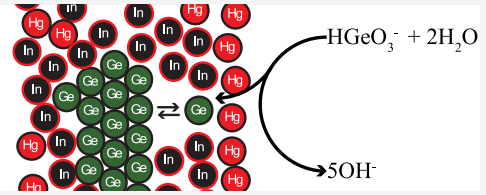


## INTRODUCTION

Liquid metals are natural media for growing inorganic crystals.[1−5] For crystalline inorganic semiconductors, elemental liquid metals in vapor–liquid–solid (VLS) and liquid-phase epitaxy (LPE) processes have been explored and utilized successfully.[6−9] In this regard, the choice of the liquid metal is known to strongly influence how the inorganic solute becomes a crystalline material. So far, the overwhelming majority of studies have focused largely on just unary liquid metals and the corresponding binary solvent/solute mixtures. Comparatively few studies have focused explicitly on exploring the composition space of liquid metal alloys to identify more optimal solvents for crystal growth. Accordingly, although the chemistry and metallurgy of liquid metal alloys have been studied intensely and even recently,[10−34] strategies that exploit this knowledge to design optimal liquid metal alloy solvents for the growth of target, crystalline inorganic materials are still lacking.

In both VLS and LPE, it is widely understood that crystal growth in a given elemental liquid metal can be improved by adding a second alloying metal to increase the solubility of the target solute.[35] The guiding rationale has been that adding elements with higher bulk solute solubilities (i.e., type A metals) into liquid metals with low bulk solute solubilities (i.e., type B metals) lowers the supersaturation attained during nucleation and crystal growth in the bulk liquid metal alloy. According to classical nucleation theory and crystal growth models,[36,37] controlling the supersaturation is the most direct way to obtain more pristine, larger solute crystals with fewer defects. This premise has been described sporadically but it is not clear if it represents the only or most impactful strategy for designing liquid metal crystal growth solvents. Specifically in VLS, it is widely accepted that the interfacial properties during the crystal growth process are important and potentially control is well established.[38−40]

Previously, identification of how a specific component alters the properties of a molten alloy during a crystal growth process was complicated by the need for high temperatures. However, a new liquid-metal-based process for growing crystalline inorganic semiconductors introduced in the past decade offers a simpler alternative.[41] Using electrochemical gradients rather than thermal gradients, the electrochemical liquid–liquid–solid (ec-LLS) strategy mirrors the nucleation and crystal growth aspects of VLS and LPE but without any heating or extensive support apparatus. Simply, a liquid metal acts as the

**Received:** November 2, 2020
**Revised:** January 14, 2021
**Published:** February 3, 2021







https://dx.doi.org/10.1021/acs.cgd.0c01485
*Cryst. Growth Des.* 2021, 21, 1645–1656

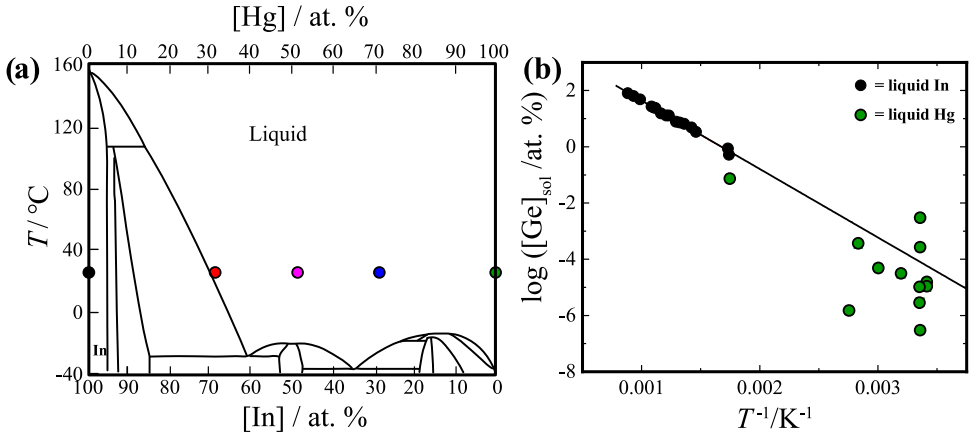


**Figure 1.** (a) Binary phase diagram for the Hg−In binary system. The colored dots represent the specific compositions of Hg−In alloys used for ec-LLS deposition of Ge in this work. Adapted with permission from Chiarenzelli, R. V. and Brown, O. L. I *Journal of Chemical and Engineering Data*, **1962**, 7(4), 477−478. Copyright 1962. (b) A plot of the known solubilities of Ge in (black dots) liquid In and in (green dots) liquid Hg as a function of reciprocal temperature. Data adapted from refs 49−50, respectively. The linear regression represents the best-fit line for the In solubility data only.

working electrode where oxidized species can be reduced and then dissolved into the liquid metal at rates dictated by the electrochemical reduction reaction, surface chemistry, and rates of dissolution.[42−45] Recent studies have shown that the liquid metal alloy composition affects the resultant crystal size and morphology,[46,47] but clear design rules for the liquid metal have yet to be identified.

In this study, the liquid Hg−In alloy system is a useful testbed for exploring and identifying aspects that may be relevant to crystal growth in ec-LLS and, by extension, to other related processes that rely on liquid metal solvents using alloys of only "type B" metals. The $Hg_{1-x}In_x$ alloy system is notable since In is a solid at room temperature but can be uniformly dissolved in Hg as a homogeneous liquid phase up to concentrations of ∼70 atom % at room temperature (Figure 1a).[48] A wide composition range of molten, liquid $Hg_{1-x}In_x$ alloys are readily accessible at room temperature just by mixing predefined amounts of each metal. Here, we use Ge as the test solute for this family of liquid metals since Ge ec-LLS by the electrochemical reduction of dissolved $GeO_2$ in water is known for both pure Hg and In nanodroplets.[41,47] Based on the available metallurgical for each metal,[49,50] the solubility of Ge in both pure In and pure Hg at room temperature is roughly of the order of $10^{-4}$ atom % (Figure 1b). Although there is some uncertainty in these data, both from extrapolation in the case of In and from Hg in the spread of the available experimental measurements,[50,51] the data clearly show that neither metal would be expected to appreciably increase the solubility of Ge in the other. Moreover, neither In nor Hg form germanicides at any temperature, and the atomic size of each metal is roughly similar (Table 1).[48,52,53] Accordingly, if bulk solute solubilities are the only important factors in designing liquid metal solvents, the expectation is that the crystallographic properties of Ge formed within every composition in the Hg−In alloy family would be the same. In contrast, these two metals differ notably in their surface properties. For example, liquid/air surface tensions for Hg and In in Table 1 differ considerably.[54,55] More importantly, the wettability of these liquid metals toward Ge are different. Hg does not readily wet a solid Ge surface, while molten In readily wets Group IV semiconductor surfaces.[56,57] In fact, molten In at elevated temperatures has been used previously to grow crystalline Ge

**Table 1. Relevant Physicochemical Properties of Hg and In**

| | Hg | In |
|---|---|---|
| atomic mass/g $mol^{-1}$ | 200.59 | 114.81 |
| gravimetric density/g $cm^{-3}$ | 13.53 | 7.02 |
| molar density/mol $cm^{-3}$ | 0.067 | 0.061 |
| atomic radius[a]/Å | 1.71 | 1.56 |
| surface tension[b]/N $m^{-1}$ | 0.47 | 0.57 |
| melting point[c]/°C | −38.3 | 156.6 |
| Ge solubility[d]/atom % | $4.6 \times 10^{-5}$[e] | $8.5 \times 10^{-5}$[f] |

[a]Data from ref 53. [b]Data are reported at the melting point in air. [c]Data from ref 48. [d]Data from refs 49, 50. [e]Average value from data reported between 20 and 25 °C. [f]Determined by linear extrapolation of data to 25 °C.

by liquid-phase epitaxy and by VLS.[56−58] Accordingly, if surface wetting of the liquid metal to solid Ge is relevant, a change in the observable crystal growth would be expected as the liquid $Hg_{1-x}In_x$ alloy composition is varied.

Herein, a series of electrochemical, materials characterization, and surface characterization data are presented to describe the Ge ec-LLS process using electrode compositions spanning the $Hg_{1-x}In_x$ family. The purpose of this work is to evaluate the hypothesis that adding In into liquid Hg will effect no change in the crystalline properties of the resultant Ge. Direct insight into the liquid metal/electrolyte interface at which the solute atoms are formed is achieved. We accomplish this by X-ray reflectivity (XRR) measurements, which provide detailed data on the local atomic structure (e.g., atomic layering)[59−61] and composition of the interface. Specifically, the angle-dependent specular X-ray reflectivities of the two central systems under study, pure liquid Hg and liquid $Hg_{0.3}In_{0.7}$ (i.e., the alloy with the highest dissolved In content) in contact with the 0.1 M $NaB_4O_7$ electrolyte solution were collected in the potential range of Ge electrodeposition. The cumulative findings are significant in the context of developing improved strategies to grow technologically important semiconductors at low temperatures.

## EXPERIMENTAL SECTION

**Materials and Chemicals.** Acetone (ACS grade, Fisher Scientific), Hg (triply distilled, D. F. Goldsmith), indium (99.99%


https://dx.doi.org/10.1021/acs.cgd.0c01485
Cryst. Growth Des. 2021, 21, 1645−1656

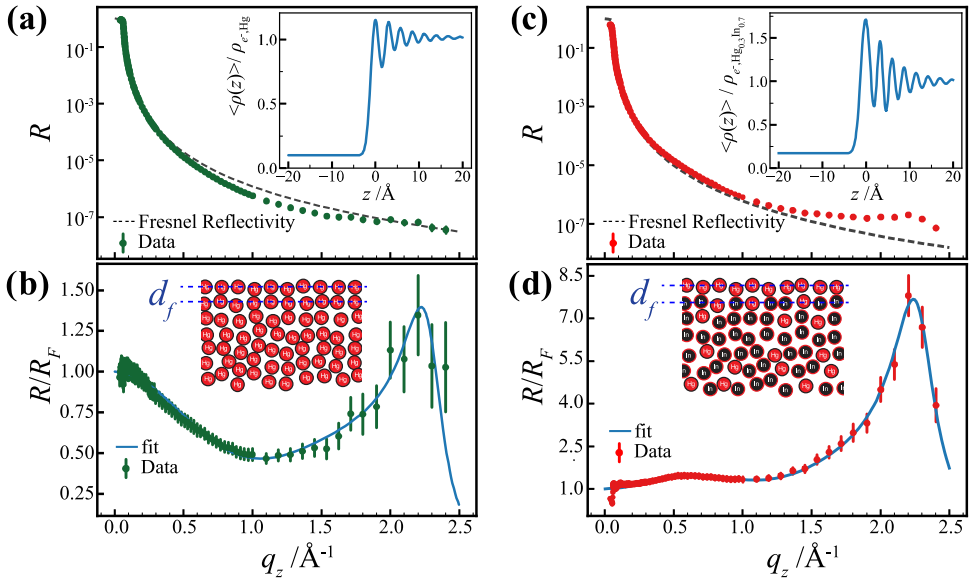


**Figure 2.** (a) Measured and (b) $R_F$-normalized X-ray reflectivity of (a, b) liquid Hg and (c, d) liquid $Hg_{0.3}In_{0.7}$ in 0.1 M $NaB_4O_7$ at a potential of −1.4 V. The dashed lines in (a, c) indicate the Fresnel reflectivity, and the solid lines in (b, d) indicate the best fit by the model described in the text. The insets in (a) and (c) are the real-space profiles of the total electron density along the surface-normal vector, while those in (b) and (d) are schematic presentations of the interface structure for each liquid metal.

Gallium Source), germanium dioxide (99.998% Sigma-Aldrich), sodium borate (>99.5% Sigma-Aldrich), indium foil (99.998%, Alfa Aesar), and Pt wire (0.25 mm diameter, Alfa Aesar) were used as received. Nanopure water with resistivity > 18.2 MΩ $cm^{-1}$ (Barnstead Nanopure) was used throughout.

**Electrochemical Details.** Both CH Instruments 420A and Solarton 1176A potentiostats were used to perform cyclic voltammetry and chronocoulometry experiments. A dual-compartment, three-electrode cell was used for all electrodepositions and consisted of a 200 $\mu$L liquid metal pool housed within a bowl and contacted from the top by an insulated Pt wire (working electrode), a graphite rod (counter electrode), and an anodized Ag wire with a AgCl coating immersed in sat. KCl in a separate fritted compartment (reference electrode). All potentials in this work are given with respect to this reference electrode. For experiments featuring solid In as the working electrode, the Pt wire contact was not used. Voltammetry experiments were performed in solutions containing either 0.01 M $NaB_4O_7$ or 0.01 M $NaB_4O_7$ with 0.05 M $GeO_2$. After electrodeposition, the electrolyte was suctioned off by hand with a pipette. Following, the liquid metal pool electrode was washed with nanopure water multiple times until residual salt crystals were no longer visible. Then, electrodeposited Ge was collected carefully from the liquid pool electrode with a clean plastic spatula, dried under $N_2$, and then characterized.

**Materials Characterization.** Scanning electron microscopy (SEM) images were obtained using a JEOL JSM-7800FLV field emission scanning electron microscope (FESEM) operating at an accelerating voltage of 10.00 kV using an in-lens ion annular secondary electron detector. X-ray diffraction spectra were collected with a Bruker D8 Advance diffractometer equipped with a Cu K$\alpha$ source, parallel beam optics, and a LynxEye detector. Raman spectra were obtained with a Tescan RISE SEM equipped with a Raman spectrometer featuring a 532 nm $Ar^+$ laser at a radiant power of 50 $\mu$W on the sample.

**X-ray Reflectivity Measurements.** X-ray reflectivity (XRR) measurements of the liquid metal/liquid electrolyte interfaces were performed using the Liquid Interface Scattering Apparatus (LISA) diffractometer[62] at beamline P08 of the PETRA III synchrotron source at DESY in Hamburg, Germany.[63] All experiments utilized a beam energy of 25 keV, corresponding to a wavelength of $\lambda$ = 0.4959 Å. The reflected intensity was recorded with a two-dimensional GaAs X-ray detector (Lambda from X-Spectrum). The detector was composed of 1536 ×512 pixels with 55 $\mu$m pixel size providing a resolution of 3.3 × $10^{-4}$ $Å^{-1}$ in both the horizontal $q_x$ and vertical $q_z$ directions. The background, due to scattering by the Hg and electrolyte bulks, was measured by offsetting the detector by 0.08° horizontally out of the plane of reflection and subtracting an area with 0.08 ° horizontal and 0.4° vertical angular acceptance, from the specular signal. A custom-designed electrochemical X-ray scattering cell with 5 cm diameter was used throughout the experiments, allowing for the injection of the $Hg_{1-x}In_x$ alloy as well as the electrolyte solution. Solutions were purged with $N_2$ gas for at least 30 min prior to injection into the cell. Liquid metal electrodes were biased for at least 15 min before each reflectivity measurement to ensure a stable interface.

In the XRR data analysis, first, the background-subtracted detector signal was normalized by the direct beam intensity and plotted versus the surface-normal scattering vector, $q_z$ ($\equiv 4\pi\lambda^{-1}\sin\alpha$). The resulting experimental X-ray reflectivity, $R(q_z)$, was normalized by the Fresnel reflectivity, $R_F(q_z)$, of a perfectly sharp interface between the liquid metal sample ($Hg_{0.3}In_{0.7}$ or Hg, respectively) and the aqueous electrolyte. Here, the critical scattering vector, $q_c$, for total external reflection at the liquid metal/electrolyte interface was determined from the difference of the total electron densities of the bulk liquid metals, $\rho_{e,Me}$, which are 3.24 $e_0Å^{-3}$ for Hg and 2.24 $e_0Å^{-3}$ for $Hg_{0.3}In_{0.7}$, and for the bulk electrolyte ($\rho_{e,H_2O}$ = 0.33 $e_0Å^{-3}$). From these values, scattering length densities of 8.177 × $10^{-5}$ $Å^{-2}$ for Hg/0.1 M $NaB_4O_7$ and 5.364 × $10^{-5}$ $Å^{-2}$ for $Hg_{0.3}In_{0.7}$/0.1 M $NaB_4O_7$ are calculated, resulting in $q_c$ values of 0.064 and 0.052 $Å^{-1}$, respectively. $R/R_F$ at each $q_z$ is a function of the laterally averaged electron density, $\langle\rho_e(z)\rangle$, profile along the surface-normal according to the master equation.[64,65] $R/R_F$ values were fitted by a modification of the distorted crystal model,[61,64] which was previously employed for the interface between liquid Hg and NaF solution.[66,67] This first-layer model treats $\langle\rho_e(z)\rangle$ of the liquid electrolyte/liquid metal junction (normalized by the bulk metal density) as a function of three independent terms, with the first describing the electrolyte, the second representing an explicit atomic layer at the interface, and the third summation term representing the decaying atomic layering in the near-surface region of the liquid metal


https://dx.doi.org/10.1021/acs.cgd.0c01485
Cryst. Growth Des. 2021, 21, 1645−1656

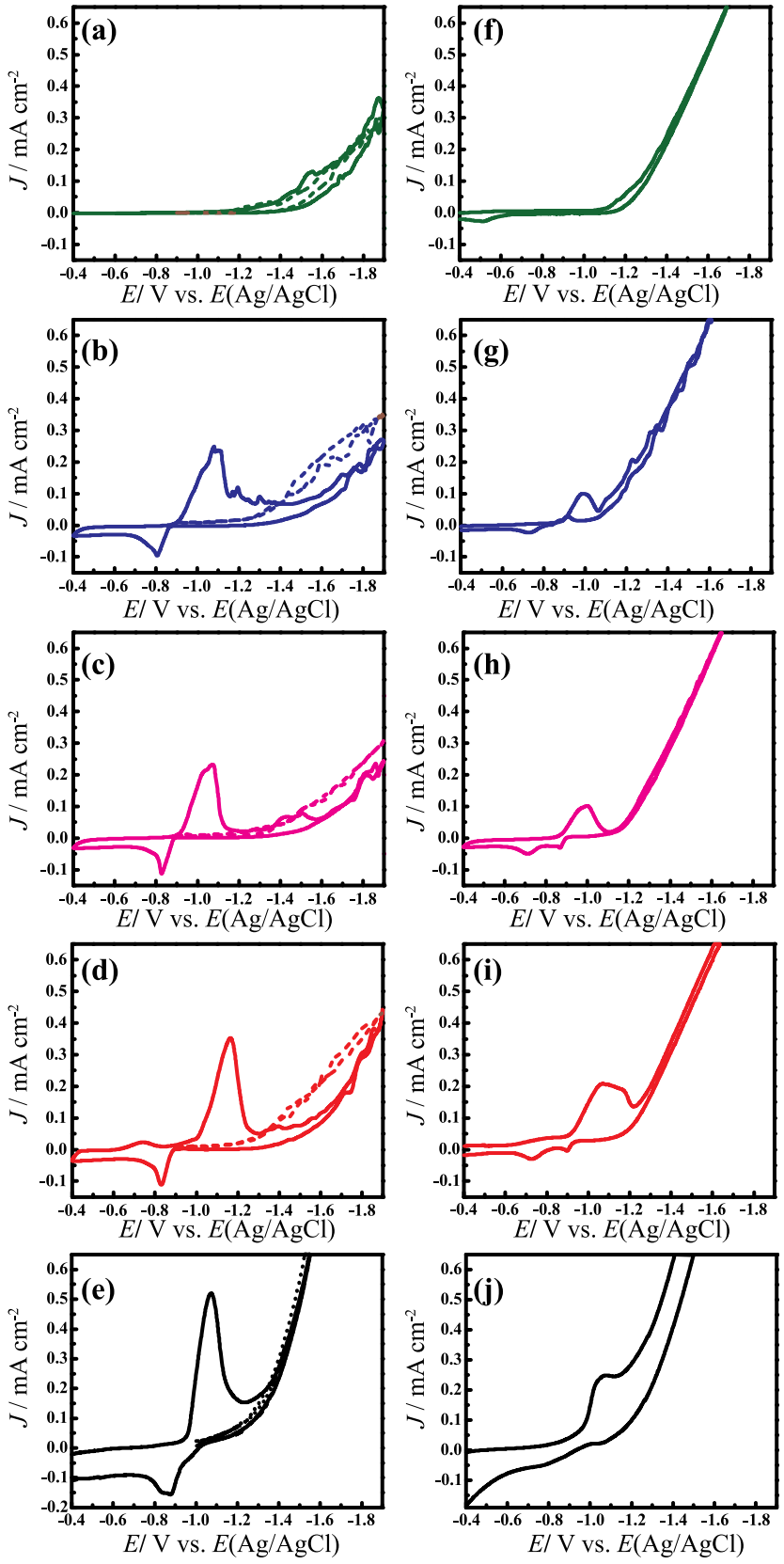


**Figure 3.** Voltammetric responses of $Hg_{1-x}In_x$ electrode immersed in 0.01 M sodium tetraborate (A−E) and a mixture of 0.01 M sodium $Na_2B_4O_7$ plus 0.05 M $GeO_2$ solution (F−J) at a scan rate of 0.01 $Vs^{-1}$. The green, blue, magenta, red, and black graphs represent the Hg, $Hg_{0.7}In_{0.3}$, $Hg_{0.5}In_{0.5}$, $Hg_{0.3}In_{0.7}$, and indium foil electrode, respectively.



https://dx.doi.org/10.1021/acs.cgd.0c01485
Cryst. Growth Des. 2021, 21, 1645−1656

$$\frac{\langle \rho_e(z) \rangle}{\rho_{e,\mathrm{Me}}} = \frac{1}{2}\frac{\rho_{e,\mathrm{H_2O}}}{\rho_{e,\mathrm{Me}}}\left(1 - \mathrm{erf}\left(\frac{z - z_{\mathrm{H_2O}}}{\sigma_{\mathrm{H_2O}}\sqrt{2}}\right)\right) + \frac{\mathrm{d}\rho_f}{\rho_{e,\mathrm{Me}}\sigma_f\sqrt{2\pi}} e^{\frac{-(z-z_f)^2}{2\sigma_f^2}} + \sum_{n=1}^{\infty} \frac{d}{\sigma_n\sqrt{2\pi}} e^{\frac{-(z-nd)^2}{2\sigma_n^2}} \quad (1)$$

Here, $z_{\mathrm{H_2O}}$ and $\sigma_{\mathrm{H_2O}}$ describe the position and width of the electrolyte front; $\rho_f$ and $\sigma_f$ are the amplitude and root-mean-square displacement of the first layer, respectively; $d$ is the atomic layer spacing after the second metal layer; $z_f$ is the position of the first layer; "$d - z_f$" is the distance between the first and second liquid metal layers; and $\sigma_n$ is the root-mean displacement of the $n$th layer, which increases with $z$ toward the liquid metal bulk and is given by $\sigma_n = \sqrt{\sigma_i^2 + n\sigma_b^2}$, where $\sigma_i$ is the intrinsic width common to all subsurface layers and $\sigma_b$ describes the rate at which $\sigma_n$ increases.[61,64]

The model was fitted to the experimental XRRs in a two-stage process, using a custom Python script. First, a global optimization was performed, with defined upper and lower bounds for each fitting parameter. Then, the resulting values were used as starting point for a local refinement. The parameters describing the electrolyte, $\sigma_{\mathrm{H_2O}}$ and $\rho_{\mathrm{H_2O}}$, had little influence on the resulting fit and thus were kept at the same values as for Hg in NaF solution.[67] The final fit was determined when $\chi^2$ was minimized below a threshold value of 0.1.

## RESULTS

**X-ray Reflectivity.** Representative XRR curves are shown in Figure 2a,c. At a low $q_z$, the measured data (circles) closely follow the corresponding Fresnel reflectivities (dashed lines), indicating that the interfaces are atomically smooth. At $q_z \geq 2$ Å$^{-1}$, a characteristic maximum is observed in both samples, which corresponds to the well-known quasi-Bragg peak associated with the atomic layering in the near-surface region of the liquid metal.[61,64,66,67]

The detailed behavior is more easily discernible after normalizing the XRR data by the Fresnel reflectivity (Figure 2b,d). For the case of pure Hg, the XRR curves in 0.1 M $NaB_4O_7$ strongly resemble those observed for the Hg/0.01 M NaF interface.[66,67] Specifically, $R(q_z)$ initially decreases up to $q_z$ = 1.2 Å$^{-1}$ and then increases again toward the quasi-Bragg peak at $q_z$ = 2.22 Å$^{-1}$. Quantitative fits to the model described in the Experimental Section provide very similar structural parameters and electron density profiles as in NaF solution at the most negative potentials (see Figure 2b and Table S1 in the Supporting Information). In particular, the first-layer density $\rho_f/\rho_{e,\mathrm{Me}}$ is very similar for Hg in $NaB_4O_7$ and in NaF.

In contrast, a very different behavior is found for the XRR of liquid $Hg_{0.3}In_{0.7}$. Here, the normalized X-ray reflectivity values initially increase, leading to a local maximum near $q_z$ = 0.6 Å$^{-1}$. Furthermore, the quasi-Bragg peak is much more pronounced. The initial increase to an $R/R_f > 1$ is indicative of a higher electron density at the surface relative to that in the bulk. Similar effects were reported for the free surfaces of other liquid metal alloys and could be explained by surface segregation of the higher-Z element.[68−70] Accordingly, the X-ray reflectivity data indicate a Hg-rich surface. This point is supported by the best fit (Figure 2d, Table S1 in the Supporting Information), which corresponded to a liquid metal surface featuring a surface layer that consists almost exclusively of Hg on top of a surface-layered bulk liquid with a composition of $Hg_{0.3}In_{0.7}$, as depicted schematically in the inset of Figure 2d. In the surface layer, the concentration of In is no greater than 0.01, whereas all following atomic layers correspond to the nominal In concentration of 0.7. This result is also in accordance with the layer spacings. At the depth of second layer and below, the fitted parameters are identical to that at the surface of molten In at 443 K,[63] which is understandable taking into account thermal expansion effects and the high In content of the $Hg_{0.3}In_{0.7}$ alloy. In contrast, the spacing of the surface layer to the subsequent layer is much larger, as expected for a layer consisting of the more bulky Hg atoms.[59,71] The decay of the atomic layering toward the liquid metal bulk is comparable to that found in pure liquid Hg and In, albeit a detailed comparison with the latter is difficult due to the differences in sample temperatures.

**Electrochemical Responses.** The voltammetric responses of Hg, $Hg_{1-x}In_x$, and In electrodes in 0.01 M $NaB_4O_7$ were examined in detail at a slow scan rate of 0.01 V s$^{-1}$ (Figure 3). Hg pool electrodes show a featureless steady-state current response when scanned between −0.4 and −1.9 V (solid green line, Figure 3a). Figure 3a also shows the response when the scan is limited to −0.9 and −1.9 V (dashed green line). $H_2$ evolution leads to some mechanical movement of the liquid metals that introduce noise in the data but the two traces are otherwise identical. Figure 3b shows similar voltammetry for $Hg_{0.7}In_{0.3}$. In this case, initiating the scan at −0.4 V resulted in a large cathodic wave with a maximum at −1.09 V and a peak current density of 0.24 mA cm$^{-2}$. Integration of this peak corresponded to a charge density of 3.86 mC cm$^{-2}$. On the return wave, anodic current onset at −0.87 V with a peak at −0.81 V and a steady-state anodic current of 0.10 mA cm$^{-2}$ at more positive potentials. Integration of this anodic current corresponded to a charge density of 0.78 mC cm$^{-2}$. When the electrode scan was initiated at −0.9 V, i.e., the electrode potential was never allowed to drift more positive than −1.0 V, the cathodic wave disappeared. Further, the current for $H_2$ evolution was consistently higher. Similar observations were noted for $Hg_{0.5}In_{0.5}$ and $Hg_{0.3}In_{0.7}$ (Figure 3d,e, respectively). The peak current densities and integrated charge densities of the cathodic wave that preceded the current onset for $H_2$ evolution when the voltammetric scan was initiated at −0. 4 V did not track monotonically with bulk In content (Table S2, Supporting Information). Data were also recorded using solid In foil as an electrode (Figure 3e). In this case, a more prominent cathodic wave was observed that again was absent when the potential was held more negative than the onset of anodic current (i.e., −1.3 V in this case). Notably, although $H_2$ bubbles were visibly observed, the current-potential response lacked any appreciable noise.

The voltammetric responses for these same electrodes at the same scan rate and initiated at −0.4 V were recorded after introduction of dissolved $GeO_2$ at a formal concentration of 0.05 M (Figure 3f–j). The principal observation was that the current at potentials more negative than −1.1 V were consistently higher, in accordance with additional current for the reduction of dissolved $GeO_2$ (i.e., $HGeO_3^- + 4e^- + 2H_2O \rightarrow Ge + 5OH^-$). From these data, a cursory estimation of the faradic efficiency for $GeO_2$ reduction at −1.4 and −1.9 V was determined (Table S2). The faradic efficiencies for $GeO_2$ reduction with $Hg_{1-x}In_x$ alloys were consistently higher than those for solid In electrodes. A second observation in these data was that the cathodic wave at more positive potentials for electrodes containing In was consistently attenuated and shifted toward more negative potential. Similarly, the anodic current profile was altered.

Figure S2 in the Supporting Information contains the amperometric responses of these electrodes for Ge ec-LLS


https://dx.doi.org/10.1021/acs.cgd.0c01485
Cryst. Growth Des. 2021, 21, 1645−1656

performed in the same electrolyte at −1.4 and −1.9 V, respectively. In every case, after the initial charging current dissipated within 100 s, the faradic current slowly decayed to different quasi-steady-state current densities. To obtain the target charge density, a total ec-LLS time between 12 500 and 75 000 s at $E$ = −1.4 V and between 3000 and 12 000 s at $E$ = −1.9 V was necessary. Notably, electrodes with lower In content took longer to reach the target charge density.

**Raman Spectral Analyses.** A black particulate Ge film completely covered the electrode surface after all Ge ec-LLS trials. Figure 4 highlights representative Raman spectra for the

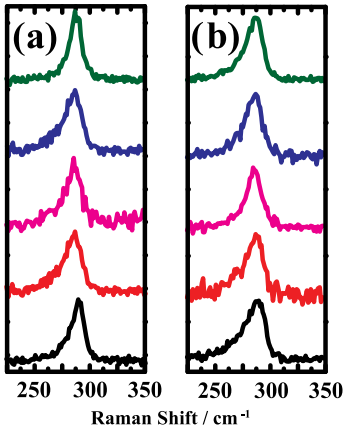


**Figure 4.** First-order Raman spectra for Ge electrodeposited on $Hg_{1-x}In_x$ electrodes immersed in 0.01 M $Na_2B_4O_7$ and 0.05 M $GeO_2$ solution and biased at −1.4 V (A) and −1.9 V (B) with respect to a Ag/AgCl reference electrode. The green, blue, magenta, red, and black graphs represent the Hg, $Hg_{0.7}In_{0.3}$, $Hg_{0.5}In_{0.5}$, $Hg_{0.3}In_{0.7}$, and indium foil electrode, respectively. The spectra have been offset for clarity.

as-deposited Ge crystallites collected with each type of electrode. The LO phonon mode for crystalline Ge near but substantially less than 300 $cm^{-1}$ was observed for every sample. Table S3 in the Supporting Information collects and summarizes the peak position and full widths at half-maximum (*fwhm*) for each ec-LLS experiment. Three general features were apparent. First, for a given electrode material, the Ge produced at −1.4 V exhibited a smaller *fwhm* value than the corresponding material produced at −1.9 V. Second, the phonon peak position for crystalline Ge prepared with pure Hg was at a larger frequency than the phonon peak positions for crystalline Ge prepared with $Hg_{1-x}In_x$. Third, the phonon peak positions tracked with In content for $Hg_{1-x}In_x$ and In electrodes.

**X-ray Diffraction Analyses.** Figure 5 shows representative power X-ray diffractograms of the ec-LLS deposited Ge crystal. The strong diffraction pattern of the as-prepared Ge crystal exhibited the reflection of diamond cubic lattice structure of crystalline Ge. Table S4 in the Supporting Information collects and summarizes the diffraction peak positions, full widths at half-maximum (*fwhm*), corresponding crystal sizes and average crystal sizes, peak intensity ratios, and lattice parameters for Hg, $Hg_{1-x}In_x$, and In electrodes at two different applied potentials. Two general characteristics were clearly visible. First, the relative intensities of the peaks in the diffractograms were not the same, indicating some change in crystal orientation or possible preferred growth direction. Second,

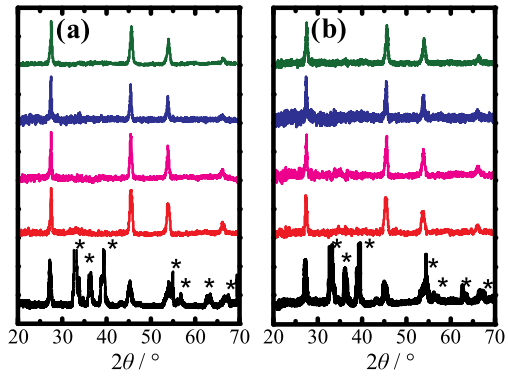


**Figure 5.** Powder X-ray diffractograms of Ge electrodeposited on Hg, $Hg_{1-x}In_x$, and In electrodes at potentials (a) −1.4 V and (b) −1.9 V under the same reaction condition, as described in this figure. Peaks denoted with * denote signals from crystalline In. The diffraction patterns are offset for clarity.

the lattice constant for Ge was clearly a function of In, increasing with the increasing amounts of In (Figure 6).

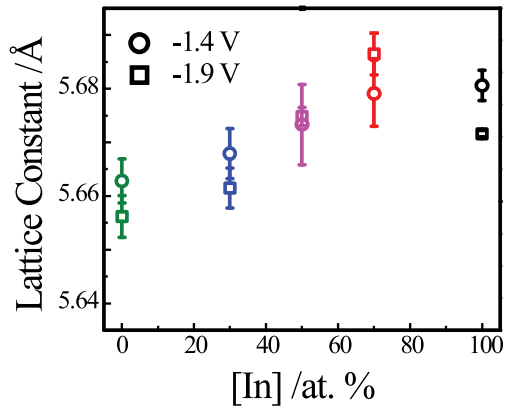


**Figure 6.** Lattice constant value of the crystalline Ge as a function of indium content (atom %) synthesized on Hg, $Hg_{1-x}In_x$, and In electrodes at potentials −1.4 V (circular dot) and −1.9 V (square dot).

**Scanning Electron Microscopy Analyses.** Representative scanning electron micrographs of as-deposited Ge crystallites for each film are presented in Figure 7. As reported previously,[41] a leaflike microstructure was observed on the Hg pool electrode (Figure 7a) at less negative potentials and a bundle of nanofibers at more negative potentials (Figure 7f).[41] However, with increasing In content in the $Hg_{1-x}In_x$ alloys (Figure 7b−d,g−i), these morphologies were not conserved. For $Hg_{0.7}In_{0.3}$, the leaflike shape was observed at both potentials, with no evidence of nanofibers. For $Hg_{0.5}In_{0.5}$, faceted grains were ∼5 μm in size and their structure was not leaflike at −1.4 V and only somewhat at −1.9 V. Additionally, sporadically interspersed in the Ge grains were smooth nanowires. For $Hg_{0.3}In_{0.7}$, the Ge grains were larger (>10 μm) at both potentials. Again, a minority fraction of Ge nanowires was intermixed throughout the ec-LLS product material. These features were in contrast to the morphologies observed with solid In electrodes (Figure 7e,j), where there were no faceted grains. Instead, the surface was coated with a contiguous, granular film with particles of ∼0.2 μm at both potentials. Smaller Ge nanowires were heterogeneously located on top of the granular surface coating. The contrasting


https://dx.doi.org/10.1021/acs.cgd.0c01485
Cryst. Growth Des. 2021, 21, 1645−1656

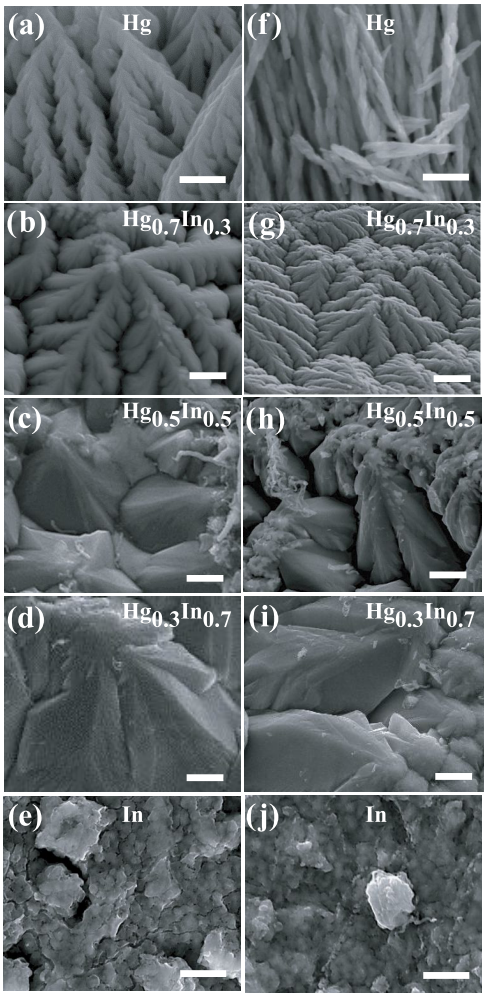


**Figure 7.** Scanning electron micrographs of as-prepared crystalline Ge electrodeposited with Hg, $Hg_{1-x}In_x$, and In electrodes from solutions containing 0.05 M $GeO_2$ and 0.01 M $Na_2B_4O_7$. Micrographs show crystalline Ge obtained at (a–e) $E = -1.4$ V and (f–j) $E = -1.9$ V vs $E$(Ag/AgCl). Scale bars: (a, f, e, j) 0.5 $\mu$m; (b, c, d, g, h, i) 1 $\mu$m.

crystalline Ge morphologies obtained with $Hg_{0.5}In_{0.5}$ and $Hg_{0.3}In_{0.7}$ are particularly notable since the total reaction time required to pass the target charge was comparable, indicating that the operative growth rates in these two cases were essentially identical, but the crystal morphology was patently different.

Figure 8 shows scanning electron micrographs specifically detailing the Ge nanowires observed with the $Hg_{0.5}In_{0.5}$, $Hg_{0.3}In_{0.7}$, and In electrodes. With the liquid $Hg_{1-x}In_x$ alloys, the Ge nanowires were several microns in length and could approach 1 $\mu$m in diameter. Additionally, these nanowires were often kinked multiple times and sometimes coiled. Almost uniformly, these nanowires featured an obvious round liquid metal cap on the tip. Elemental analysis indicated that the compositions of these caps were 52.6% In, 14.5% Hg, 20.2% Ge, and 12.6% O. For crystalline Ge electrodeposited with solid In electrodes, the nanowires were notably shorter and much smaller in diameter (~0.1 $\mu$m) but still exhibited numerous kinks.

## DISCUSSION

The presented data support two primary points. First, the surface of $Hg_{1-x}In_x$ alloys is enriched by Hg but only in the topmost atomic layer of the liquid metal. Second, the presence of In during Ge ec-LLS did not alter the nucleation and crystal growth rates but did accelerate the diffusion of Ge along the growing crystal surface, greatly impacting the resultant crystal morphology. These points are discussed below.

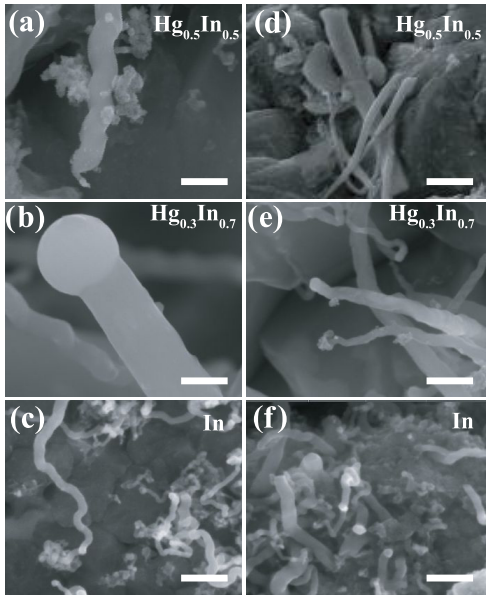


**Figure 8.** SEM micrographs of as-synthesized Ge crystal electrodeposited on $Hg_{1-x}In_x$ from the 0.1 M $Na_2B_4O_7$ and 0.05 M $GeO_2$ solution. (a–c) Potential: −1.4; (d–f) potential: −1.9 V vs Ag/AgCl. Scale bars: 0.5 $\mu$m.

**Surface Composition of Liquid $Hg_{1-x}In_x$ Alloys.** The surface composition of an ideal liquid metal mixture can be determined from the Gibbs adsorption isotherm. Specifically, in an ideal mixture, the component with the higher surface energy will have a more dilute fractional composition on the surface relative to its fractional composition in the bulk mixture[72]

$$x_s = \frac{1}{\frac{1-x_b}{x_b} e^{\frac{-A}{k_B T}(\gamma_{Hg}-\gamma_{In})} + 1} \quad (2)$$

where $x_b$ is the bulk composition of In in the binary alloy; $\gamma_{In}$ and $\gamma_{Hg}$ are the surface tensions for In and Hg, respectively; $A$ is the average area per atom in the binary liquid alloy; $k_B$ is the Boltzmann constant; and $T$ is the temperature. To estimate accurately the surface composition of $Hg_{1-x}In_x$ alloys immersed in aqueous sodium tetraborate, the potential dependence of the surface tensions for each pure liquid metal in this electrolyte is required. Nevertheless, from surface tensions of In and Hg relative to vacuum (Table 1), the general expectation is that the surface of $Hg_{1-x}In_x$ alloys should be largely composed of Hg (e.g., $x_s \sim 0.3$ when $x_b = 0.7$).[73] The X-ray reflectance data directly confirm this concept, i.e., even the HgIn alloy with the highest bulk In content is Hg-rich at the electrolyte/liquid metal interface. Additionally, the collected XRR data provide further structural insight, i.e., the bulk composition is maintained just beneath the outer, Hg-rich surface layer.

Although XRR data were collected at a single electrolyte composition, the observed surface features of $Hg_{1-x}In_x$ should not depend strongly on the concentration of the supporting electrolyte. The best fit of the XRR data showed no evidence


https://dx.doi.org/10.1021/acs.cgd.0c01485
Cryst. Growth Des. 2021, 21, 1645−1656

that adsorption of the supporting electrolyte occurs at the negative potentials of interest. No suitable fit was possible that included an explicit adlayer at potentials relevant to ec-LLS. Moreover, the background ion concentration does not appreciably change the electron density of the electrolyte, further limiting the impact of concentration on the XRR interpretation. The electrochemical data corroborate the inferences from the X-ray data. In the blank electrolyte without dissolved $GeO_2$, all of the liquid $Hg_{1-x}In_x$ alloy electrodes exhibited $H^+$ reduction current-potential profiles consistent with the behavior of pure Hg rather than In electrodes. Since the electrochemical reduction of $H^+$ to $H_2$ is an inner-sphere redox process that depends strongly on the electronic character of the electrode surface, these data are fully in line with these liquid metals possessing a surface layer of predominantly/exclusively Hg atoms.

The electrochemical data separately indicate that In atoms are still able to participate in interfacial processes. The appearance of the cathodic redox wave near −1.1 V for $Hg_{1-x}In_x$ alloys strongly mirrors the reduction of the surface oxide on pure In,[74] even for $Hg_{0.7}In_{0.3}$. The integrated charge under these curves constituted several monolayers worth of indium oxide, indicating that the subsurface In atoms are readily oxidized in these $Hg_{1-x}In_x$ liquid metal alloys. The exact mechanism of how subsurface In atoms are oxidized is not presently clear, but the occurrence and reoccurrence of indium oxidation suggest $x_s \neq 0$, in line with the estimate of $x_s \leq 0.02$ from the X-ray data. In this case, the oxidation of In atoms "getters" $In^0$ from the surface, which are then rapidly replaced by the ample supply of subsurface In. If the supply rate of In atoms to the electrolyte/liquid metal surface influences the rate of In oxide formation, then a difference in electrochemical behaviors at positive potentials would be expected. However, the return sweeps in the voltammetry in Figure 4b−d exhibit oxidation peaks with equivalent positions and profiles. Accordingly, the exchange rate between surface and subsurface atomic layers is not assumed to be limiting in the reactivity of In atoms at the electrolyte/electrode interface.

The collective data highlight beneficial properties of the $Hg_{1-x}In_x$/electrolyte interface structure for the electrochemical reduction of dissolved $GeO_2$ and Ge incorporation into the liquid metal, i.e., the first two steps of the ec-LLS process. Because of the strong Hg surface segregation, the electrode surface is Hg-like, substantially reducing the hydrogen evolution current density and facilitating higher coulombic efficiency of the ec-LLS process. The limitation of the Hg enrichment to a single atomic layer at the surface is likewise advantageous relative to a shallow gradient in the liquid metal composition. The steep Hg enrichment only at the surface ensures a high In content already very near to the surface. Thus, the beneficial influence of In on the Ge transport (vide infra) becomes effective directly following Ge entering the subsurface of the liquid metal phase. In addition, our observations indicate that the surface segregation layer is highly dynamic and apparently does not represent a barrier for the transfer of species between the interior of the liquid metal and the electrode/electrolyte interface.

**Influence of $Hg_{1-x}In_x$ Composition on Ge Crystal Growth by ec-LLS.** The cumulative microscopic, Raman, and X-ray diffraction data separately suggest that inclusion of In in liquid Hg specifically changed the fate of Ge atoms after initial electroreduction of dissolved $GeO_2$. Ge crystals grown with pure Hg exhibited clear dendritic structures, consistent with fast nucleation and crystal growth occurring at a large supersaturation. That is, because the solubility of Ge in Hg is small at room temperature, any appreciable amount of Ge dissolved in the liquid metal likely resulted in a large supersaturation, as observed in related ec-LLS processes.[75,76] Since the rates of nucleation and crystal growth are typically proportional to the extent of supersaturation,[77−79] the subsequent crystal growth rates are expected to be correspondingly fast.

When In was included in liquid Hg, especially at low concentrations, the dendritic structure of the resultant Ge crystals was still evident. This feature is consistent with the fact that the supersaturation attained during ec-LLS remained unchanged because In did not increase the bulk solubility of Ge in the liquid metal. However, the electron micrographs are clear that each Ge dendritic branch became progressively thicker with increasing In content. Eventually, the apparent grain size still had the outer profile of the dendrite "leafs" but effectively with the inner void space filled in.

As described in Figure 9, we posit this observation arises because In can access the crystal growth front and because the presence of In specifically enhances the mobility of Ge along the solid Ge surface. The precedent for In acting as a surface transporter is not known in electrochemical settings but is well established in the field of vapor deposition of semiconductor films.[80,81] In this latter context, In has been identified as a "surfactant" that specifically facilitates Ge surface diffusion in the case of vapor-phase deposition of Ge on Si substrates.[82−84] A notable difference between this prior precedence of In as a surface transporting agent and the work shown here is the operating temperatures. For vapor-phase deposition, the action of In at a surface is typically understood at elevated temperatures. For the work shown here, the influence of In as a surface transporting agent was observed at room temperature.

The notion of In as an agent that affects/catalyzes the surface transport of Ge is consistent with the other materials characterization data. Specifically, the inferred crystallite sizes from the X-ray diffraction data do not appreciably change when In is dissolved in Hg, consistent with the idea that In is not changing the supersaturation level of Ge in the liquid metal and the corresponding crystal growth rate. Similarly, the Raman spectra are consistently red-shifted for all liquid metals, indicating that even though large apparent Ge grains are obtained with higher In content, the Ge grains are polycrystalline with crystallite domains remaining below the Bohr exciton radius of Ge (i.e., 25 nm).[85]

Presumably, the mediated transport of Ge by In involves a strong interaction between In and Ge. There are no known stable In-Ge complexes in the reported binary phase diagram[49] that would predict the formation of a strong In-Ge bond. However, molten In at elevated temperatures completely wets crystalline Ge,[57,58] indicating that the surface tension of the In/Ge interface is small. Although no direct measurement of the surface tension at this interface is available, an estimate of 0.58 N $m^{-1}$ at $T$ = 25 °C is possible through Young's equation and Eötvös' rule.[57] By comparison, the surface tension of the Hg/Ge interface at room temperature is in excess of 1.1 N $m^{-1}$, since the solid/vapor surface tensions of crystalline Ge are uniformly in excess of this value[86] and the wetting contact angle between Hg and a Ge wafer is significantly greater than 90 °. These liquid/solid surface tensions, by eq 2, would now predict an accumulation of In at the liquid metal/Ge crystal


https://dx.doi.org/10.1021/acs.cgd.0c01485
Cryst. Growth Des. 2021, 21, 1645−1656

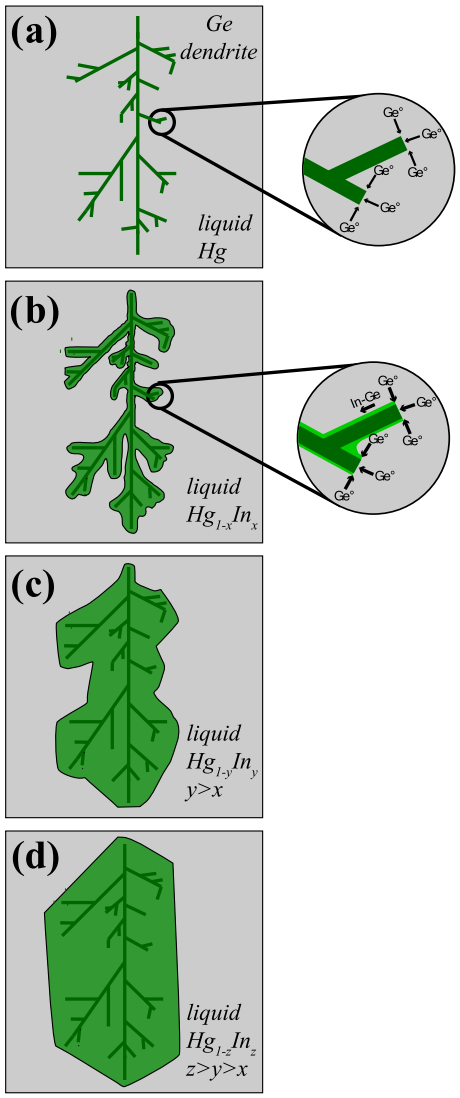


**Figure 9.** Schematic depiction of the influence of In on the surface diffusion of Ge on the resultant morphology of the Ge crystallites as a function of In concentration.

interface. Accordingly, the obvious trend in increasing Ge lattice constants with increasing In content in liquid $Hg_{1-x}In_x$ alloys in the X-ray diffraction patterns is consistent with the premise that the crystal growth plane is In-rich. Separately, the observation that the liquid metal droplets on the observed Ge nanowires consistently had a decreased fraction of In relative to the bulk pool alloy composition, in conjunction with the measurable In concentrations in these Ge nanowires, indicating that In had a high affinity for Ge.

The action of In as a surface transporting agent is also in accordance with a recent and separate observation from our group on the growth mechanism of Ge nanowires using molten In nanodroplets.[46] In that work, the cumulative data indicated that Ge crystal growth was limited by the surface transport of Ge to the growth interface. That work also implied that electrodeposition of crystalline Ge using solid, rather than liquid, In electrodes may be possible. Here, in this work, we in fact did detect some accumulation of crystalline Ge with solid In foil electrodes. This observation stands in stark contrast to our and other groups' past attempts to perform crystalline Ge electrodeposition with solid metal electrodes.[41,87,88] However, the size of these Ge crystallites were smaller than for the liquid metal electrodes, their arrangement was a thin, compact film, and the total quantity was small. Hence, although fast mobility of electrodeposited Ge atoms on an In surface may still occur, this feature alone is not sufficient to mimic the crystal growth process in ec-LLS.

## CONCLUSIONS

This work rejects the hypothesis that bulk solubilities of solutes are the only relevant factors in choosing components in the design of a liquid metal solvent for growing tailored inorganic crystals. Instead, this work demonstrates that the inclusion of In in binary $Hg_{1-x}In_x$ liquid metal alloys strongly impacts the morphology of the resultant Ge crystals grown by ec-LLS. In pure Hg, the dendritic structure of the resultant Ge crystals reflects the low Ge solubility and high operative supersaturations during nucleation and growth. Upon addition of In into Hg, the dendritic structures still form initially but then are "filled in" with more Ge crystallites. The separate voltammetric and X-ray reflective data indicate that Hg is strongly enriched in the first atomic layer of $Hg_{1-x}In_x$ but that the alloy beneath this surface layer maintains the bulk composition, enabling In to still participate in interfacial processes while surficial Hg otherwise facilitates the initial electroreduction step for ec-LLS over $H_2$ generation. The inferred take away is that once Ge is dissolved beneath the first atomic layer of the liquid metal, In acts to accelerate Ge diffusion along the solid Ge/liquid metal interface. These data suggest that In as a liquid metal component specifically can dictate the crystalline grain morphology by effecting transport at the growth interface rather than by changing the solute solubility. More generally, the data argue for further development of liquid metal alloys as optimal solvents since surface segregation can improve the interfacial properties relevant for crystal growth.

## ASSOCIATED CONTENT

### Supporting Information

The Supporting Information is available free of charge at https://pubs.acs.org/doi/10.1021/acs.cgd.0c01485.

Chronoamperometric responses for Hg, $Hg_{1-x}In_x$, and In electrodes immersed in 10 mM $Na_2B_4O_7$ and 50 mM $GeO_2$ solution, a tabulated collection of the fitting parameters used in the first-layer model for analysis of the X-ray reflectivity data presented in the main text as well as the corresponding values for two relevant comparison fits for liquid Hg and liquid In previously reported in the literature, a tabulated summary of the voltammetric features of the data presented in the main text, a tabulated summary of the Raman spectral features shown in the main text, and a tabulated summary of the X-ray diffraction data (PDF)

## AUTHOR INFORMATION

### Corresponding Authors

**Olaf Magnussen** − *Institute for Experimental and Applied Physics and Ruprecht Haensel Laboratory, Kiel University, D-24118 Kiel, Germany;* orcid.org/0000-0003-4900-0880; Phone: +49-431-880.5579; Email: magnussen@physik.uni-kiel.de

**Stephen Maldonado** − *Department of Chemistry and Program in Applied Physics, University of Michigan, Ann Arbor, Michigan 48109-1055, United States;* orcid.org/



https://dx.doi.org/10.1021/acs.cgd.0c01485
Cryst. Growth Des. 2021, 21, 1645−1656

0000-0002-2917-4851; Phone: +1-734-647-4750; Email: smald@umich.edu; http://www.umich.edu/~mgroup/

### Authors

**Dhruba Pattadar** − *Department of Chemistry, University of Michigan, Ann Arbor, Michigan 48109-1055, United States*
**Quintin Cheek** − *Department of Chemistry, University of Michigan, Ann Arbor, Michigan 48109-1055, United States*
**Andrea Sartori** − *Institute for Experimental and Applied Physics, Kiel University, D-24118 Kiel, Germany*
**Yifan Zhao** − *Department of Chemistry, University of Michigan, Ann Arbor, Michigan 48109-1055, United States*
**Rajendra P. Giri** − *Institute for Experimental and Applied Physics, Kiel University, D-24118 Kiel, Germany*
**Bridget Murphy** − *Institute for Experimental and Applied Physics and Ruprecht Haensel Laboratory, Kiel University, D-24118 Kiel, Germany;* orcid.org/0000-0002-1354-2381

Complete contact information is available at: https://pubs.acs.org/10.1021/acs.cgd.0c01485

### Notes

The authors declare no competing financial interest.

## ■ ACKNOWLEDGMENTS

The authors acknowledge generous financial support from the National Science Foundation (CHE-1807755) for S.M. and from the Deutsche Forschungsgemeinschaft (Ma1618/18) and the German Federal Ministry for Science and Education (05K16FK2 and 05K19K2) for O.M.M. and B.M.M., respectively. They also thank the beamline staff at P08 of PETRA III for experimental support and DESY for the beamtime.

## ■ REFERENCES

(1) Kanatzidis, M. G.; Pöttgen, R.; Jeitschko, W. The Metal Flux: A Preparative Tool for the Exploration of Intermetallic Compounds. *Angew. Chem. Int. Ed.* **2005**, *44*, 6996−7023.
(2) Stojanovic, M.; Latturner, S. E. Growth of New Ternary Intermetallic Phases from Ca/Zn Eutectic Flux. *J. Solid State Chem.* **2007**, *180*, 907−914.
(3) Benbow, E. M.; Dalal, N. S.; Latturner, S. E. Crystal Growth and Magnetic Behavior of R6t13−Xalxmy Phases (R = La, Nd; T = Mn, Fe; M = Main Group) Grown from Lanthanide-Rich Eutectic Fluxes. *J. Solid State Chem.* **2009**, *182*, 3055−3062.
(4) Sebastian, C. P.; Malliakas, C. D.; Chondroudi, M.; Schellenberg, I.; Rayaprol, S.; Hoffmann, R.-D.; Pöttgen, R.; Kanatzidis, M. G. Indium Flux-Growth of Eu2auge3: A New Germanide with an Alb2 Superstructure. *Inorg. Chem.* **2010**, *49*, 9574−9580.
(5) He, H.; Tyson, C.; Saito, M.; Bobev, S. Synthesis and Structural Characterization of the Ternary Zintl Phases Ae3al2pn4 and Ae3ga2pn4 (Ae = Ca, Sr, Ba, Eu; Pn = P, as). *J. Solid State Chem* **2012**, *188*, 59−65.
(6) Seifner, M. S.; Sistani, M.; Zivadinovic, I.; Bartmann, M. G.; Lugstein, A.; Barth, S. Drastic Changes in Material Composition and Electrical Properties of Gallium-Seeded Germanium Nanowires. *Cryst. Growth Des.* **2019**, *19*, 2531−2536.
(7) Ouyang, L.; Maher, K. N.; Yu, C. L.; McCarty, J.; Park, H. Catalyst-Assisted Solution−Liquid−Solid Synthesis of Cds/Cdse Nanorod Heterostructures. *J. Am. Chem. Soc.* **2007**, *129*, 133−138.
(8) Trentler, T. J.; Hickman, K. M.; Goel, S. C.; Viano, A. M.; Gibbons, P. C.; Buhro, W. E. Solution-Liquid-Solid Growth of Crystalline Iii-V Semiconductors: An Analogy to Vapor-Liquid-Solid Growth. *Science* **1995**, *270*, 1791−1794.
(9) Schmidt, V.; Wittemann, J. V.; Gösele, U. Growth, Thermodynamics, and Electrical Properties of Silicon Nanowires. *Chem. Rev.* **2010**, *110*, 361−388.
(10) Sar, F.; Gasser, J. G. Electronic Transport Properties of Liquid Ga-Zn Alloys. *Intermetallics* **2003**, *11*, 1369−1376.
(11) Turchanin, A.; Freyland, W. Surface Freezing and Wetting in Ga-Pb Alloy: Second Harmonic and Plasma Generation Study. *Phys. Chem. Chem. Phys.* **2003**, *5*, 5285−5290.
(12) Scharmann, F.; Cherkashinin, G.; Breternitz, V.; Knedlik, C.; Hartung, G.; Weber, T.; Schaefer, J. A. Viscosity Effect on Gainsn Studied by Xps. *Surf. Interface Anal.* **2004**, *36*, 981−985.
(13) Xi, Y.; Zu, F. Q.; Li, X. F.; Yu, J.; Liu, L. J.; Li, Q.; Chen, Z. H. High-Temperature Abnormal Behavior of Resistivities for Bi-in Melts. *Phys. Lett. A* **2004**, *329*, 221−225.
(14) Shpyrko, O. G.; Grigoriev, A. Y.; Streitel, R.; Pontoni, D.; Pershan, P. S.; Deutsch, M.; Ocko, B.; Meron, M.; Lin, B. H. Atomic-Scale Surface Demixing in a Eutectic Liquid Bisn Alloy. *Phys. Rev. Lett.* **2005**, *95*, No. 106103.
(15) Yazdanpanah, M. M.; Harfenist, S. A.; Safir, A.; Cohn, R. W. Selective Self-Assembly at Room Temperature of Individual Free-standing Ag2ga Alloy Nanoneedles. *J. Appl. Phys.* **2005**, *98*, No. 073510.
(16) Shpyrko, O. G.; Streitel, R.; Balagurusamy, V. S. K.; Grigoriev, A. Y.; Deutsch, M.; Ocko, B. M.; Meron, M.; Lin, B. H.; Pershan, P. S. Surface Crystallization in a Liquid Ausi Alloy. *Science* **2006**, *313*, 77−80.
(17) Dickey, M. D.; Chiechi, R. C.; Larsen, R. J.; Weiss, E. A.; Weitz, D. A.; Whitesides, G. M. Eutectic Gallium-Indium (Egain): A Liquid Metal Alloy for the Formation of Stable Structures in Microchannels at Room Temperature. *Adv. Funct. Mater.* **2008**, *18*, 1097−1104.
(18) Yatsenko, S. P.; Sabirzyanov, N. A.; Yatsenko, A. S. in Dissolution Rates and Solubility of Some Metals in Liquid Gallium and Aluminum, *13th International Conference on Liquid and Amorphous Metals*, 2008; pp U654−U660.
(19) Cheng, S.; Rydberg, A.; Hjort, K.; Wu, Z. Liquid Metal Stretchable Unbalanced Loop Antenna. *Appl. Phys. Lett.* **2009**, *94*, No. 144103.
(20) Egry, I.; Ricci, E.; Novakovic, R.; Ozawa, S. Surface Tension of Liquid Metals and Alloys - Recent Developments. *Adv. Colloid Interface Sci.* **2010**, *159*, 198−212.
(21) Khalouk, K.; Mayoufi, M.; Gasser, J. G. Are There Phase Transitions in Liquid Metallic Alloys? *Philos. Mag.* **2010**, *90*, 2695−2709.
(22) Wang, L.-M.; Tian, Y.; Liu, R. Dependence of Glass Forming Ability on Liquid Fragility: Thermodynamics Versus Kinetics. *Appl. Phys. Lett.* **2010**, *97*, No. 181901.
(23) Deshpande, R. D.; Li, J.; Cheng, Y.-T.; Verbrugge, M. W. Liquid Metal Alloys as Self-Healing Negative Electrodes for Lithium Ion Batteries. *J. Electrochem. Soc.* **2011**, *158*, A845−A849.
(24) Jeyakumar, M.; Hamed, M.; Shankar, S. Rheology of Liquid Metals and Alloys. *J. Non-Newtonian Fluid Mech.* **2011**, *166*, 831−838.
(25) Liu, T.; Sen, P.; Kim, C.-J. C. J. Characterization of Nontoxic Liquid-Metal Alloy Galinstan for Applications in Microdevices. *J. Microelectromech. Syst.* **2012**, *21*, 443−450.
(26) Thelen, J.; Dickey, M. D.; Ward, T. A Study of the Production and Reversible Stability of Egain Liquid Metal Microspheres Using Flow Focusing. *Lab Chip* **2012**, *12*, 3961−3967.
(27) Agarwal, R.; Samui, P.; Kulkarni, S. G. Thermodynamic Investigations of (Bi+Ni) System - Part Ii. *J. Chem. Thermodyn.* **2013**, *57*, 477−484.
(28) Kramer, R. K.; Majidi, C.; Wood, R. J. Masked Deposition of Gallium-Indium Alloys for Liquid-Embedded Elastomer Conductors. *Adv. Funct. Mater.* **2013**, *23*, 5292−5296.
(29) Boley, J. W.; White, E. L.; Chiu, G. T. C.; Kramer, R. K. Direct Writing of Gallium-Indium Alloy for Stretchable Electronics. *Adv. Funct. Mater.* **2014**, *24*, 3501−3507.
(30) Föttinger, K.; Rupprechter, G. In Situ Spectroscopy of Complex Surface Reactions on Supported Pd-Zn, Pd-Ga, and Pd(Pt)-Cu Nanoparticles. *Acc. Chem. Res.* **2014**, *47*, 3071−3079.

(31) Wang, K.; Jiang, K.; Chung, B.; Ouchi, T.; Burke, P. J.; Boysen, D. A.; Bradwell, D. J.; Kim, H.; Muecke, U.; Sadoway, D. R. Lithium-Antimony-Lead Liquid Metal Battery for Grid-Level Energy Storage. *Nature* **2014**, *514*, 348.
(32) Melchakov, S. Y.; Yamshchikov, L. F.; Osipenko, A. G.; Pozdeev, P. A.; Rusakov, M. A. Solubility and Excessive Thermodynamic Characteristics of Pr and Nd in the Ga-Sn Eutectic Alloy. *Russ. Metall.* **2015**, 595−598.
(33) Zavabeti, A.; et al. A Liquid Metal Reaction Environment for the Room-Temperature Synthesis of Atomically Thin Metal Oxides. *Science* **2017**, *358*, 332−335.
(34) Zhao, X.; Xu, S.; Liu, J. Surface Tension of Liquid Metal: Role, Mechanism and Application. *Front. Energy* **2017**, *11*, 535−567.
(35) Biswas, S.; O'Regan, C.; Petkov, N.; Morris, M. A.; Holmes, J. D. Manipulating the Growth Kinetics of Vapor−Liquid−Solid Propagated Ge Nanowires. *Nano Lett.* **2013**, *13*, 4044−4052.
(36) Kubota, N.; Yokota, M.; Mullin, J. W. Supersaturation Dependence of Crystal Growth in Solutions in the Presence of Impurity. *J. Cryst. Growth* **1997**, *182*, 86−94.
(37) Vekilov, P. G. Nucleation. *Cryst. Growth Des.* **2010**, *10*, 5007−5019.
(38) Jacobsson, D.; Panciera, F.; Tersoff, J.; Reuter, M. C.; Lehmann, S.; Hofmann, S.; Dick, K. A.; Ross, F. M. Interface Dynamics and Crystal Phase Switching in Gaas Nanowires. *Nature* **2016**, *531*, 317−322.
(39) Tornberg, M.; Maliakkal, C. B.; Jacobsson, D.; Dick, K. A.; Johansson, J. Limits of Iii−V Nanowire Growth Based on Droplet Dynamics. *J. Phys. Chem. Lett.* **2020**, *11*, 2949−2954.
(40) Wen, C. Y.; Tersoff, J.; Hillerich, K.; Reuter, M. C.; Park, J. H.; Kodambaka, S.; Stach, E. A.; Ross, F. M. Periodically Changing Morphology of the Growth Interface in Si, Ge, and Gap Nanowires. *Phys. Rev. Lett.* **2011**, *107*, No. 025503.
(41) Carim, A. I.; Collins, S. M.; Foley, J. M.; Maldonado, S. Benchtop Electrochemical Liquid−Liquid−Solid Growth of Nanostructured Crystalline Germanium. *J. Am. Chem. Soc.* **2011**, *133*, 13292−13295.
(42) Zhang, T.; Fahrenkrug, E.; Maldonado, S. Electrochemical Liquid-Liquid-Solid Deposition of Ge at Hg Microdroplet Ultramicroelectrodes. *J. Electrochem. Soc.* **2016**, *163*, D500−D505.
(43) Fahrenkrug, E.; Gu, J.; Jeon, S.; Veneman, P. A.; Goldman, R. S.; Maldonado, S. Room-Temperature Epitaxial Electrodeposition of Single-Crystalline Germanium Nanowires at the Wafer Scale from an Aqueous Solution. *Nano Lett.* **2014**, *14*, 847−852.
(44) Fahrenkrug, E.; Biehl, J.; Maldonado, S. Electrochemical Liquid−Liquid−Solid Crystal Growth of Germanium Microwires on Hard and Soft Conductive Substrates at Low Temperature in Aqueous Solution. *Chem. Mater.* **2015**, *27*, 3389−3396.
(45) Ma, L.; Fahrenkrug, E.; Gerber, E.; Crowe, A. J.; Venable, F.; Bartlett, B. M.; Maldonado, S. High-Performance Polycrystalline Ge Microwire Film Anodes for Li Ion Batteries. *ACS Energy Lett.* **2017**, *2*, 238−243.
(46) Cheek, Q.; Fahrenkrug, E.; Hlynchuk, S.; Alsem, D. H.; Salmon, N. J.; Maldonado, S. In Situ Transmission Electron Microscopy Measurements of Ge Nanowire Synthesis with Liquid Metal Nanodroplets in Water. *ACS Nano* **2020**, *14*, 2869−2879.
(47) Mahenderkar, N. K.; Liu, Y.-C.; Koza, J. A.; Switzer, J. A. Electrodeposited Germanium Nanowires. *ACS Nano* **2014**, *8*, 9524−9530.
(48) Okamoto, H. Hg-in (Mercury-Indium). *J. Phase Equilib. Diffus.* **2012**, *33*, 159−160.
(49) Olesinki, R. W.; Kanani, N.; Abbaschian, G. J. The Ge-in (Germanium-Indium) System. *Bull. Alloy Phase Diagrams* **1985**, *6*, 536−539.
(50) Guminski, C. The Ge-Hg (Germanium-Mercury) System. *J. Phase Equilib.* **1999**, *20*, 344.
(51) Keck, P. H.; Broder, J. The Solubility of Silicon and Germanium in Gallium and Indium. *Phys. Rev.* **1953**, *90*, 521−522.
(52) Grosse, A. A. V. The Relationship between Surface Tension and Energy of Liquid Metals and Their Heat of Vaporization at the Melting Point. *J. Inorg. Nucl. Chem.* **1964**, *26*, 1349−1361.
(53) Clementi, E.; Raimondi, D. L.; Reinhardt, W. P. Atomic Screening Constants from Scf Functions. Ii. Atoms with 37 to 86 Electrons. *J. Chem. Phys.* **1967**, *47*, 1300−1307.
(54) White, D. W. G. The Surface Tensions of Indium and Cadmium. *Metall. Mater. Trans. B* **1972**, *3*, 1933−1936.
(55) Wilkinson, M. C. The Surface Properties of Mercury. *Chem. Rev.* **1972**, *72*, 575−625.
(56) Zolper, J. C.; Barnett, A. M. Selective Area Solution Growth of Ge and Gaas on Si. *J. Appl. Phys.* **1989**, *66*, 210−214.
(57) Teubner, T.; Boeck, T.; Schmidt, K. Modelling of Solution Growth of Silicon from Small Indium Droplets − Homogeneous Nucleation. *J. Cryst. Growth* **1999**, *198−199*, 425−429.
(58) Maruyama, T.; Matsuda, K.; Naritsuka, S. Multinuclear Layer-by-Layer Growth on Ge(111) by Lpe. *J. Cryst. Growth* **2005**, *275*, e2155−e2160.
(59) DiMasi, E.; Tostmann, H.; Ocko, B. M.; Pershan, P. S.; Deutsch, M. X-Ray Reflectivity Study of Temperature-Dependent Surface Layering in Liquid Hg. *Phys. Rev. B: Condens. Matter Mater. Phys.* **1998**, *58*, R13419−R13422.
(60) Elsen, A.; Festersen, S.; Runge, B.; Koops, C. T.; Ocko, B. M.; Deutsch, M.; Seeck, O. H.; Murphy, B. M.; Magnussen, O. M. In Situ X-Ray Studies of Adlayer-Induced Crystal Nucleation at the Liquid−Liquid Interface. *Proc. Natl. Acad. Sci. U.S.A.* **2013**, *110*, 6663.
(61) Magnussen, O. M.; Ocko, B. M.; Regan, M. J.; Penanen, K.; Pershan, P. S.; Deutsch, M. X-Ray Reflectivity Measurements of Surface Layering in Liquid Mercury. *Phys. Rev. Lett.* **1995**, *74*, 4444−4447.
(62) Murphy, B. M.; Greve, M.; Runge, B.; Koops, C. T.; Elsen, A.; Stettner, J.; Seeck, O. H.; Magnussen, O. M. A Novel X-Ray Diffractometer for Studies of Liquid-Liquid Interfaces. *J. Synchrotron Radiat.* **2014**, *21*, 45−56.
(63) Seeck, O. H.; et al. The High-Resolution Diffraction Beamline P08 at Petra Iii. *J. Synchrotron Radiat.* **2012**, *19*, 30−38.
(64) Pershan, P. S.; Schlossman, M. *Liquid Surfaces and Interfacs: Synchrotron X-Ray Methods*; Cambridge University Press:Cambridge, 2012.
(65) Robinson, L. K. Structure Factor Determination in Surface X-Ray Diffraction. *Aust. J. Phys.* **1988**, *41*, 359−368.
(66) Elsen, A.; Murphy, B. M.; Ocko, B. M.; Tamam, L.; Deutsch, M.; Kuzmenko, I.; Magnussen, O. M. Surface Layering at the Mercury-Electrolyte Interface. *Phys. Rev. Lett.* **2010**, *104*, No. 105501.
(67) Runge, B.; Festersen, S.; Koops, C. T.; Elsen, A.; Deutsch, M.; Ocko, B. M.; Seeck, O. H.; Murphy, B. M.; Magnussen, O. M. Temperature- and Potential-Dependent Structure of the Mercury-Electrolyte Interface. *Phys. Rev. B: Condens. Matter Mater. Phys.* **2016**, *93*, No. 165408.
(68) Yang, B.; Li, D.; Rice, S. A. Structure of the Liquid-Vapor Interface of a Dilute Ternary Alloy: Pb and in in Ga. *Phys. Rev. B: Condens. Matter Mater. Phys.* **2003**, *67*, No. 054203.
(69) Tostmann, H.; Dimasi, E.; Shpyrko, O. G.; Pershan, P. S.; Ocko, B. M.; Deutsch, M. Ii. Surface and Interfacial Phenomena: Surface Phases in Binary Liquid Metal Alloys: An X-Ray Study. *Ber. Bunsengesellschaft Phys. Chem.* **1998**, *102*, 1136−1141.
(70) Regan, M. J.; Pershan, P. S.; Magnussen, O. M.; Ocko, B. M.; Deutsch, M.; Berman, L. E. X-Ray Reflectivity Studies of Liquid Metal and Alloy Surfaces. *Phys. Rev. B: Condens. Matter Mater. Phys.* **1997**, *55*, 15874−15884.
(71) Tostmann, H.; DiMasi, E.; Pershan, P. S.; Ocko, B. M.; Shpyrko, O. G.; Deutsch, M. Surface Structure of Liquid Metals and the Effect of Capillary Waves: X-Ray Studies on Liquid Indium. *Phys. Rev. B: Condens. Matter Mater. Phys.* **1999**, *59*, 783−791.
(72) Dumke, M. F.; Tombrello, T. A.; Weller, R. A.; Housley, R. M.; Cirlin, E. H. Sputtering of the Gallium-Indium Eutectic Alloy in the Liquid Phase. *Surf. Sci.* **1983**, *124*, 407−422.
(73) Oguchi, Y.; Itami, T.; Shimoji, M. Surface Tension of the Liquid Hg-in Alloys. *Phys. Chem. Liq.* **1981**, *10*, 315−325.


https://dx.doi.org/10.1021/acs.cgd.0c01485
*Cryst. Growth Des.* 2021, 21, 1645−1656

(74) Metikoš-Huković, M.; Omanović, S. Thin Indium Oxide Film Formation and Growth: Impedance Spectroscopy and Cyclic Voltammetry Investigations. *J. Electroanal. Chem.* **1998**, *455*, 181−189.
(75) Cheek, Q.; Fahrenkrug, E.; Hlynchuk, S.; Alsem, D. H.; Salmon, N. J.; Maldonado, S. In Situ Transmission Electron Microscopy Measurements of Ge Nanowire Synthesis with Liquid Metal Nanodroplets in Water. *ACS Nano* **2020**, *14*, 2869−2879.
(76) DeMuth, J.; Fahrenkrug, E.; Maldonado, S. Controlling Nucleation and Crystal Growth of Ge in a Liquid Metal Solvent. *Cryst. Growth Des.* **2016**, *16*, 7130−7138.
(77) De Yoreo, J. J.; Vekilov, P. G. Principles of Crystal Nucleation and Growth. *Rev. Mineral. Geochem.* **2003**, *54*, 57−93.
(78) Kodambaka, S.; Tersoff, J.; Reuter, M. C.; Ross, F. M. Germanium Nanowire Growth Below the Eutectic Temperature. *Science* **2007**, *316*, 729.
(79) Senthil Pandian, M.; Verma, S.; Pareek, P.; Ramasamy, P.; Bartwal, K. S. Laser Shadowgraphy and Mach-Zehnder Interferometric Imaging of Convection, Concentration and Growth Kinetics During Unidirectional Solution Growth of Benzophenone Crystal. *Opt. Laser Technol.* **2020**, *132*, No. 106491.
(80) Won, D.; Weng, X.; Redwing, J. M. Effect of Indium Surfactant on Stress Relaxation by V-Defect Formation in Gan Epilayers Grown by Metalorganic Chemical Vapor Deposition. *J. Appl. Phys.* **2010**, *108*, No. 093511.
(81) Won, D.; Weng, X.; Redwing, J. M. Metalorganic Chemical Vapor Deposition of N-Polar Gan Films on Vicinal Sic Substrates Using Indium Surfactants. *Appl. Phys. Lett.* **2012**, *100*, No. 021913.
(82) Eaglesham, D. J.; Unterwald, F. C.; Jacobson, D. C. Growth Morphology and the Equilibrium Shape: The Role of "Surfactants" in Ge/Si Island Formation. *Phys. Rev. Lett.* **1993**, *70*, 966−969.
(83) Minoda, H.; Tanishiro, Y.; Yamamoto, N.; Yagi, K. In Situ Tem Observations of Surfactant-Mediated Epitaxy: Growth of Ge on an Si(111) Surface Mediated by In. *Surf. Sci.* **1996**, *357*−*358*, 418−421.
(84) Voigtländer, B.; Zinner, A.; Weber, T.; Bonzel, H. P. Modification of Growth Kinetics in Surfactant-Mediated Epitaxy. *Phys. Rev. B: Condens. Matter Mater. Phys.* **1995**, *51*, 7583−7591.
(85) Vadavalli, S.; Valligatla, S.; Neelamraju, B.; Dar, M. H.; Chiasera, A.; Ferrari, M.; Desai, N. R. Optical Properties of Germanium Nanoparticles Synthesized by Pulsed Laser Ablation in Acetone. *Front. Phys.* **2014**, *2*, 57.
(86) Zhang, J.-M.; Ma, F.; Xu, K.-W.; Xin, X.-T. Anisotropy Analysis of the Surface Energy of Diamond Cubic Crystals. *Surf. Interface Anal.* **2003**, *35*, 805−809.
(87) Bui, N. N.; Ledina, M.; Reber, T. J.; Jung, J.; Stickney, J. L. Electrochemical Scanning Tunneling Microscopic Study of the Potential Dependence of Germanene Growth on Au(111) at Ph 9.0. *ACS Nano* **2017**, *11*, 9481−9489.
(88) Liang, X.; Kim, Y.-G.; Gebergziabiher, D. K.; Stickney, J. L. Aqueous Electrodeposition of Ge Monolayers. *Langmuir* **2010**, *26*, 2877−2884.


https://dx.doi.org/10.1021/acs.cgd.0c01485
*Cryst. Growth Des.* 2021, 21, 1645−1656